ELSEVIER

Journal of Fluids and Structures 19 (2004) 747–763

JOURNAL OF FLUIDS AND STRUCTURES

www.elsevier.nl/locate/jnlabr/yjfls

Effects of structural nonlinearity on subsonic aeroelastic characteristics of an aircraft wing with control surface

J.-S. Bae[a,*], D.J. Inman[a], I. Lee[b]

[a] *Department of Mechanical Engineering, Center for Intelligent Material Systems and Structures, Virginia Polytechnic Institute and State University, 310 Durham Hall, Blacksburg, VA 24061, USA*

[b] *Department of Aerospace Engineering, Korea Advanced Institute of Science and Technology, 373-1 Guseong-dong, Yuseong-gu, Daejeon 305-701, South Korea*

Received 1 April 2003; accepted 15 April 2004

Abstract

The nonlinear aeroelastic characteristics of an aircraft wing with a control surface are investigated. A doublet-hybrid method is used for the calculation of subsonic unsteady aerodynamic forces and the minimum-state approximation is used for the approximation of aerodynamic forces. A free vibration analysis is performed using the finite element and the fictitious mass methods. The structural nonlinearity in the control surface hinge is represented by both free-play and a bilinear nonlinearity. These nonlinearities are linearized using the describing function method. From the nonlinear flutter analysis, various types of limit cycle oscillations and periodic motions are observed in a wide range of air speeds below the linear flutter boundary. The effects of structural nonlinearities on aeroelastic characteristics are investigated.

1. Introduction

Flutter is a dynamic aeroelastic instability that involves aerodynamic, inertial, and elastic forces of a flight vehicle. If flutter occurs in flight, the aircraft structure may fail. Therefore, it is important to predict the aeroelastic characteristics accurately to prevent aeroelastic instabilities such as flutter.

During the past decades, most aeroelastic analyses of flight vehicles have been performed under the assumption of structural linearity. Under this assumption, the aeroelastic characteristics can be easily obtained. However, the aeroelastic results under the assumption of structural linearity may not agree with the physical phenomena because real structures have structural nonlinearities such as free-play, bilinearity, asymmetry, and hysteresis.

Typically, nonlinear aeroelastic responses include flutter, divergence, limit cycle oscillation (LCO) and chaotic motion. When a linear system becomes unstable, the amplitude of the response increases exponentially, whereas a nonlinear system has bounded motion such as LCO or chaotic motion which occur above or below the linear flutter speed. Although both LCO and chaotic motion do not cause the catastrophic failure of a structure, these motions can cause a structure to be damaged by fatigue and can considerably effect the control systems of flight vehicles. Thus, the effects of structural nonlinearities on the aeroelastic characteristics of flight vehicles should be investigated in the design stage of a flight vehicle.

Nonlinear aeroelastic analyses of a wing with concentrated nonlinearities have been performed by several investigators. Woolston et al. (1957) analyzed a relatively simple system including free-play, hysteresis, and cubic

*Corresponding author. Tel.: +1-540-231-2906.

E-mail addresses: jsbae@vt.edu (J.-S. Bae), dinman@vt.edu (D.J. Inman), inlee@asdl.kaist.ac.kr (I. Lee).

0889-9746/$ - see front matter
doi:10.1016/j.jfluidstructs.2004.04.005

Nomenclature

a	stiffness ratio
A	LCO amplitude
b	reference length, half chord
$[C]$	damping matrix
$[GC]$	generalized damping matrix
$[GK]$	generalized stiffness matrix
$[GM]$	generalized mass matrix
$\{f\}$	nonlinear term
$\{F(s)\}$	Laplace transforms of $\{f\}$
$[K]$	stiffness matrix
$[K_n]$	nonlinear stiffness matrix
K_θ	flap hinge stiffness
$[M]$	mass matrix
q	dynamic pressure
$[\underline{Q}]$	aerodynamic influence coefficient matrix
s	Laplace variable
$\{u\}$	displacement vector
$\{\underline{u}\}$	modal displacement vector
U	air speed
x_a	augmented state by aerodynamic approximation
$X(s)$	Laplace transforms of x
$X_a(s)$	Laplace transforms of x_a
δ	free-play
θ	flap angle
ρ	air density
$[\phi]$	modal matrix

Subscripts

n	nonlinear
θ	flap angle

nonlinearity, and showed that LCO may occur below the linear flutter boundary. Laurenson and Trn (1980) studied flutter of a missile control surface with structural nonlinearities using the Describing Function Method. Lee (1986) developed an iterative scheme for multiple nonlinearities using the describing function method and the structural dynamics modification method. Yang and Zhao (1988) studied the LCO of a typical section model with pitch nonlinearity subject to incompressible flow using the Theodorsen function. Lee and Tron (1989) studied the flutter characteristics of a CF-18 aircraft with structural nonlinearities in the leading-edge flap hinge and the wing-fold hinge using the Describing Function Method. Hauenstein et al. (1990) and Zara et al. (1992) analytically and experimentally studied the nonlinear aeroelastic response of a rigid wing with a structural nonlinearity. Lee and Kim (1995) studied LCO and chaotic motion of a missile control surface with free-play nonlinearity using time-domain analysis.

Conner et al. (1997) and Tang et al. (1999) numerically and experimentally studied the nonlinear aeroelastic characteristics of a typical section with control surface free-play in incompressible flow. This study showed that the jumps of LCO amplitudes were observed. Virgin et al. (1999) studied the chaotic motion of a typical section and Tang et al. (2000) studied the nonlinear responses of an airfoil excited by a gust load. Sheta et al. (2002) conducted computational and experimental investigations of a nonlinear aeroelastic system with a fifth-order polynomial spring.

Recently, Bae et al. (2002) studied the nonlinear flutter characteristics of a wing with a control surface using frequency- and time-domain analyses. It was shown that LCO and chaotic motion are observed in a wide range of air speeds below the linear boundary and the coupling between flapping mode and other flexible modes are important in the aeroelastic characteristics. Bae and Lee (2004) studied the LCO characteristics of a two-dimensional model and showed that the LCOs can be observed above or below the linear flutter boundary dependent on the frequency ratio between plunge and pitch modes. Bae et al. (2004) studied the nonlinear aeroelasticity of a deployable missile control fin

and showed that the aeroelastic characteristics can become more stable than in the case of linear aeroelasticity due to the nonlinearity of a deployable hinge.

The purpose of the present study is to investigate the effects of structural nonlinearities in the control surface hinge on the aeroelastic characteristics of an aircraft wing. The present study is a continuation of the previous work by Bae et al. (2002). The authors intend to improve the previous aeroelastic analysis method and investigate the effects of nonlinear type and an initial condition on the aeroelastic characteristics. In the present study, the finite element method (MSC, 1981) is used for the free vibration analysis and the modal approach using Fictitious Mass method (FM) (Karpel and Newman, 1988) is used to reduce the problem size and the computation time. The Doublet-Hybrid Method (DHM) (Ueda and Dowell 1982; Evesman and Pitt, 1991) is used for the computation of subsonic unsteady aerodynamic forces and Minimum-State Approximation (MSA) of Karpel (1982) is used to approximate the unsteady aerodynamic forces. Structural nonlinearity is linearized using the describing function method. The root-locus method and the time-integration method are used for the nonlinear aeroelastic analysis. The nonlinear aeroelastic characteristics and boundaries of an aircraft wing with free-play and bilinear nonlinearities are studied.

2. Theoretical analysis

2.1. Aeroelastic equation

The aeroelastic equation with a structural nonlinearity can be written as

$$[M]\{\ddot{u}\} + [C]\{\dot{u}\} + [K_n(u)]\{u\} = \{F(t, u, \dot{u})\}, \tag{1}$$

where $[M]$, $[C]$, $[K_n]$, and $\{u\}$ are the mass matrix, damping matrix, stiffness matrix with structural nonlinearities, aerodynamic force vector, and deflection vector, respectively. For a piecewise nonlinearity, the restoring force term, $[K_n(u)]\{u\}$, can be written as follows:

$$[K_n(u)]\{u\} = [K]\{u\} + \{f(u)\}, \tag{2}$$

where $[K]$ is a linear stiffness matrix without structural nonlinearity, and $\{f(u)\}$ is the restoring force vector whose elements are zero except for the nonlinear contribution.

2.2. Fictitious mass method

In general, aeroelastic analyses are conducted in the generalized modal coordinates to save computational time and memory. If structural nonlinearities are present in the structure, then the modal approach may not be used. This is because the use of the constant modal coordinates of the nominal structure can give inaccurate results and may require a relatively large number of modes in order to achieve a reasonable level of accuracy. To overcome this problem, the FM method (Karpel and Newman, 1988) is used here. The idea of the FM method is that the local deformation due to the large mass enables us to examine the structural variation. This method provides an efficient and easy way to apply the computational scheme.

Ignoring the damping and aerodynamic force terms in Eq. (1), the free vibration equations of an n DOF system loaded with fictitious mass is written

$$[M + M_f]\{\ddot{u}\} + [K]\{u\} = \{0\}. \tag{3}$$

The elements of the FM matrix $[M_f]$ are zero except for the degrees of freedom where structural variations, like structural nonlinearities, occur. From the normal mode analysis of Eq. (3), we can obtain a set of n fictitious mass modes $[\phi]$, and then, the generalized mass and stiffness matrices are given as

$$[GM_f] = [\phi]^{\mathrm{T}}[M + M_f][\phi], \tag{4}$$

$$[GK_f] = [\phi]^{\mathrm{T}}[K][\phi] = [\omega_f^2], \tag{5}$$

where $[\omega_f^2]$ is a diagonal matrix of the natural frequencies, including zero frequencies for rigid-body modes. Using the FM modes ($\{u\} = [\phi]\{\xi\}$), the free vibration equation of an actual structure with structural variation $[\Delta K]$ can be written as

$$([GM_f] - [\phi]^{\mathrm{T}}[M_f][\phi])\{\ddot{\xi}\} + ([GK_f] + [\phi]^{\mathrm{T}}[\Delta K][\phi])\{\xi\} = \{0\}. \tag{6}$$

The mode shapes of the FM method are transformed to the basic structure and the new basic mode shapes serve as a constant set of generalized coordinates throughout the aeroelastic analysis. The papers by Bae et al. (2002) and Karpel and Newman (1988) can be referred to for more detailed descriptions for the FM method.

2.3. Unsteady aerodynamic influence coefficients

Using the modal matrix $[\phi]$ obtained from the FM model, the structural displacements can be transformed into modal coordinates as follows:

$$\{u\} = [\phi]\{\underline{u}\}, \tag{7}$$

where $\{\underline{u}\}$ is the displacement in modal coordinates. Then, the generalized aerodynamic forces can be written as

$$\{\underline{F}\} = [\phi]^{\mathrm{T}}\{F\} = q[\phi]^{\mathrm{T}}[\underline{Q}][\phi]\{\underline{u}\} = q[\underline{Q}]\{\underline{u}\}, \tag{8}$$

where $q = \frac{1}{2}\rho U^2$ and $[\underline{Q}]$ are the dynamic pressure and the generalized aerodynamic influence coefficient (AIC) matrix, respectively. Generally, the generalized aerodynamic influence coefficients are calculated for tabled reduced frequencies with an unsteady aerodynamic technique such as a panel method and computational fluid dynamic method. In the present study, DHM code (Bae, 2002) is used for the computation of the subsonic unsteady AIC in Eq. (8). Panel methods like DHM are to calculate the relation between the pressure difference at the doublet point and downwash at the receiving point using a kernel function. The generalized AIC $[\underline{Q}]$ is a function of Mach number and the reduced frequency. Hence, if supersonic region is considered, a supersonic panel method like supersonic doublet-point method must be used to calculate the AIC.

Using the transformation in Eq. (7), the aeroelastic equation in Eq. (1) can be transformed into the generalized coordinates as follows:

$$[GM]\{\underline{\ddot{u}}\} + [GC]\{\underline{\dot{u}}\} + [GK]\{\underline{u}\} = q[\underline{Q}]\{\underline{u}\} - [\phi]^{\mathrm{T}}\{f(u)\}, \tag{9}$$

where the generalized mass, damping, and stiffness matrix are written as

$$[GM] = [GM_f] - [\phi]^{\mathrm{T}}[M_f][\phi], \tag{10}$$

$$[GC] = [\phi]^{\mathrm{T}}[C][\phi], \tag{11}$$

$$[GK] = [GK_f] + [\phi]^{\mathrm{T}}[\Delta K][\phi]. \tag{12}$$

2.4. State-space form of aeroelastic equation

To integrate the aeroelastic equations in Eq. (9), a transformation is applied to obtain state-space equations. The generalized AIC matrix $[\underline{Q}]$ in Eq. (8) should be approximated by a rational function because it is a function of the tabulated reduced frequencies. There are many methods for rational function approximation (RFA). The present analysis uses Karpel's MSA (Karpel, 1982) method. The approximation form of Karpel's method is as follows:

$$[Q(s)] = [P_1]\left(\frac{b}{U}\right)^2 s^2 + [P_2]\left(\frac{b}{U}\right)s + [P_3] + [D](s[I] - [\bar{R}])^{-1}[E]s, \tag{13}$$

where $[P_i]$, $[D]$, and $[E]$ are calculated from a least-squares fit and $[\bar{R}]$ is a diagonal matrix. The diagonal terms of $[\bar{R}]$ are the aerodynamic poles and constants to be determined for the best fit of $[\underline{Q}]$.

Using Laplace transformation and MSA, Eq. (5) can be written as

$$([\bar{M}]s^2 + [\bar{C}]s + [\bar{K}])\{\underline{U}(s)\} = [\bar{D}]\{X_a(s)\} - [\phi]^{\mathrm{T}}\{F(s)\}, \tag{14}$$

where

$$[\bar{M}] = [GM] - \tfrac{1}{2}\rho b^2[P_1], \quad [\bar{C}] = [GC] - \tfrac{1}{2}\rho Ub[P_2], \tag{15a, b}$$

$$[\bar{K}] = [GK] - \tfrac{1}{2}\rho U^2[P_3], \quad [\bar{D}] = \tfrac{1}{2}\rho U^2[D]. \tag{15c, d}$$

The state vector $X_a(s)$ in Eq. (14) is obtained as

$$\{X_a(s)\} = (s[I] - [\bar{R}])^{-1}[E]s\{X(s)\}. \tag{16}$$

Defining the new state v as $\dot{\underline{u}}$, the final state-space aeroelastic equations are obtained as

$$\begin{Bmatrix} \dot{v} \\ \dot{\underline{u}} \\ \dot{x}_a \end{Bmatrix} = \begin{bmatrix} -[\bar{M}]^{-1}[\bar{C}] & -[\bar{M}]^{-1}[\bar{K}] & -[\bar{M}]^{-1}[\bar{D}] \\ [I] & [0] & [0] \\ [E] & [0] & [\bar{R}] \end{bmatrix} \begin{Bmatrix} v \\ \underline{u} \\ x_a \end{Bmatrix} + \begin{Bmatrix} -[\bar{M}]^{-1}[\phi]^{\mathrm{T}}\{f\} \\ 0 \\ 0 \end{Bmatrix}. \tag{17}$$

2.5. Root-locus method and time simulation

Generally, there are two kinds of aeroelastic analysis methods, frequency-domain method and time-domain method. Frequency-domain method includes conventional $V-g$ method, $p-k$ method (MacNeal-Schwendler Corp, 1981), and root-locus method, and time-domain method requires the time-integration of Eq. (18). Although the approaches of these methods are different, they provide similar aeroelastic solutions for linear aeroelastic problems.

The advantages of frequency-domain analysis are that it requires relatively less computation time, allows for a simple analysis procedure, and provides results that are easily interpreted. The drawback to this method is that it cannot be directly applied to nonlinear aeroelastic problem. For a harmonic motion like LCO, a nonlinear spring can be linearized with describing function method. Unlike the frequency-domain method, time-domain method can be applied to nonlinear aeroelastic problems. However, the time-domain method requires complex analysis procedures and large computation times, and may produce results that are difficult to interpret. Therefore, both methods are necessary for efficient nonlinear aeroelastic analysis. The present aeroelastic analysis procedure is (i) to perform the frequency-domain analysis using an equivalent spring and to establish LCO boundary (ii) to simulate aeroelastic responses based on the results of frequency-domain analysis.

In the present study, the root-locus method and time integration method are used for nonlinear aeroelastic analysis. The root-locus method involves tracing the root-loci of Eq. (18). As the air speed U increases, a real part of eigenvalue of Eq. (18) is changed from negative to positive. This point is the flutter point, and the speed U is the flutter speed U_f. To integrate Eq. (18), the Runge–Kutta method is used here.

2.6. Linearization of nonlinear hinge spring

Fig. 1 shows a fighter wing with a control surface like flaperon. A servoactuator is connected at the root of a control surface as shown in Fig. 1. Due to manufacturing tolerances or loosened mechanical linkages, the connection between a control surface and a servoactuator may have some nonlinearities. For analysis purpose, the nonlinearities can be represented by a nonlinear hinge spring.

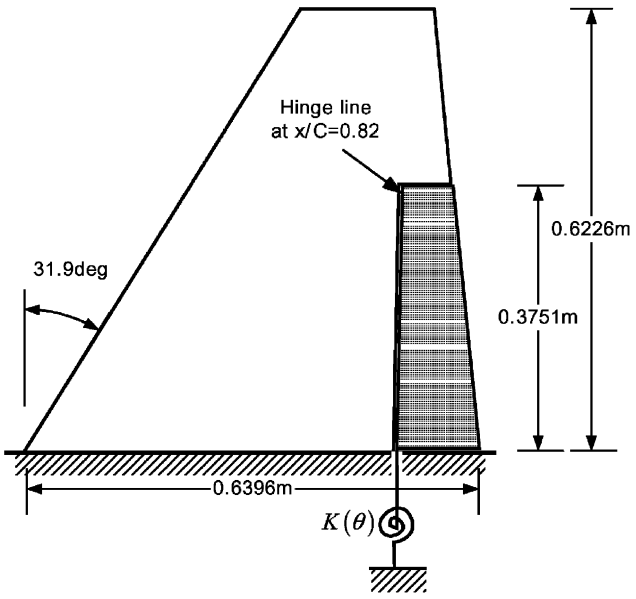

Fig. 1. Configuration of aircraft wing with control surface.

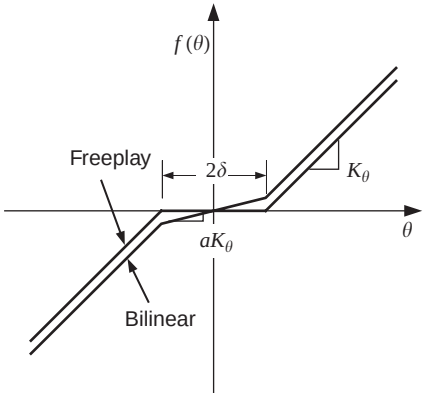

Fig. 2. Free-play and bilinear spring.

The elements of $\{f\}$ in Eq. (18) are zero except for the element representing force exerted by the nonlinear hinge spring of a control surface. This element can be represented by free-play or bilinear nonlinearity. Fig. 2 shows a bilinear spring. The bilinear spring can be expressed as

$$f(\theta) = \begin{cases} K_\theta[\theta - (1-a)\delta], & \theta > \delta, \\ aK_\theta\theta, & -\delta < \theta < \delta, \\ K_\theta[\theta + (1-a)\delta], & \theta < -\delta, \end{cases} \tag{18}$$

where θ and δ are a flap rotation angle and free-play, respectively. When the stiffness ratio a is zero, Eq. (11) represents a nonlinear spring with free-play.

For frequency-domain analysis, we need to obtain the equivalent spring from the bilinear spring in Eq. (19). The main idea of the describing function method is to calculate the equivalent spring under the assumption of a harmonic motion. If the motion of the flap angle θ is harmonic, we can write this as

$$\theta = A\sin\omega t, \tag{19}$$

where A and ω are the amplitude and frequency of harmonic motion, respectively. Considering only the fundamental component, the restoring force can be written as

$$f(\theta) = K_{eq}\theta, \tag{20}$$

$$K_{eq} = \begin{cases} aK_\theta, & 0 \leqslant A < \delta, \\ \dfrac{K_\theta}{\pi}\left[\pi - 2(1-a)\sin^{-1}\dfrac{\delta}{A} - (1-a)\sin\left(2\sin^{-1}\dfrac{\delta}{A}\right)\right], & A \geqslant \delta. \end{cases} \tag{21}$$

Fig. 3 shows the relationship between the LCO amplitude of an aeroelastic responses and the equivalent stiffness. As shown in Fig. 3, the equivalent stiffness of a nonlinear spring decreases considerably compared with that of a linear spring and the equivalent stiffness increases as the LCO amplitude increases. The equivalent stiffness of a bilinear spring is larger than that of free-play and the aeroelastic characteristics of a bilinear spring are predicted to be better than those of free-play.

3. Numerical example and discussion

As a numerical example, the aircraft wing with a control surface shown in Fig. 1 is used. The material is aluminum. The material properties of the aluminum used are $E = 72\,\text{GPa}$, $\rho_{al} = 2800\ \text{kg/m}^3$, and $v = 0.33$. The thickness of the wing is 6 mm.

3.1. Free vibration analysis

Table 1 shows the natural frequencies of the aircraft wing with a control surface using both the direct method and the FM method. The hinge stiffness used in the free vibration analysis is 400 N m/rad. With the direct method, the aircraft wing is directly modelled with a control surface hinge spring, whereas with the FM method, it is modelled with an FM

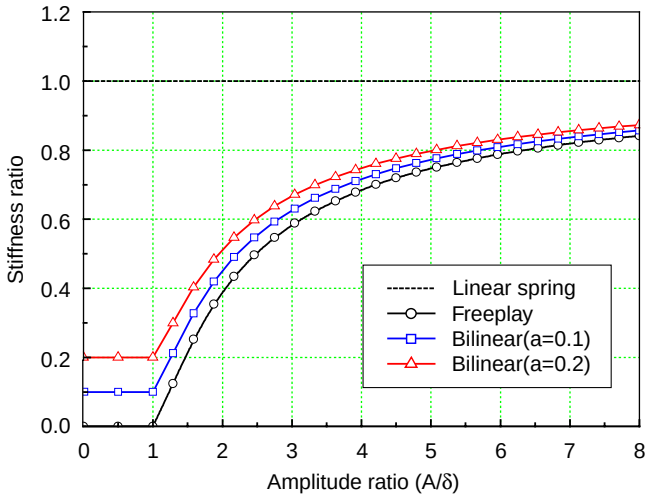

Fig. 3. Equivalent stiffness of nonlinear spring.

Table 1
Comparison of natural frequencies ($K_\theta = 400$ N m/rad)

Mode no.	Direct method	Fictitious mass method				
		4	6	8	10	12
1	15.61	15.61	15.61	15.61	15.61	15.61
2	52.79	53.58	52.80	52.80	52.79	52.79
3	64.33	65.66	64.34	64.33	64.33	64.33
4	86.38	113.39	86.41	86.39	86.38	86.38
5	164.5		164.5	164.5	164.5	164.5
6	212.3		558.2	212.4	212.3	212.3
7	266.4			268.6	266.6	266.5
8	306.9			772.2	307.0	307.0
9	319.3				319.5	319.4
10	425.3				1304.0	425.3
11	436.8					437.1
12	514.3					1565.9

and without a hinge spring in the finite element analysis. After the finite element analysis, the FM model is established by adding a hinge spring. Although a hinge spring has structural variations, it is sufficient to change the stiffness of the hinge only. For the hinge stiffness of 400 N m/rad, the lowest four natural frequencies of the direct method and FM method agree well except for the highest mode. This disagreement is due to the local distortion in the highest mode caused by an added FM. In general, the lowest two modes (bending and torsion modes) are important for a wing without a control surface and the lowest four modes are important for a wing with a control surface. Hence, the lowest eight modes are used in the proceeding aeroelastic analysis. Fig. 4 shows the natural frequency variations and the mode shapes of the lowest four modes for a change in hinge stiffness. Independent of hinge stiffness, the FM method provides accurate results. There are two points where noticeable mode shapes changes are observed. One is approximately 20 N m/rad and the other is approximately 300 N m/rad. The variation of the flapping mode is very large. Its effect moves from the first mode to second mode and from second mode to the third mode. As the hinge stiffness increases, the frequencies and the mode shapes of the lowest four modes vary significantly but the higher modes have little variation.

3.2. Aeroelastic analysis (linear case)

Table 2 shows a comparison of flutter speed and frequency using the $V-g$ method (Bae, 2002), the root-locus method, and the time-integration method. In these cases, the Mach number is 0.7 and the air density is 1.23 kg/m^3. The

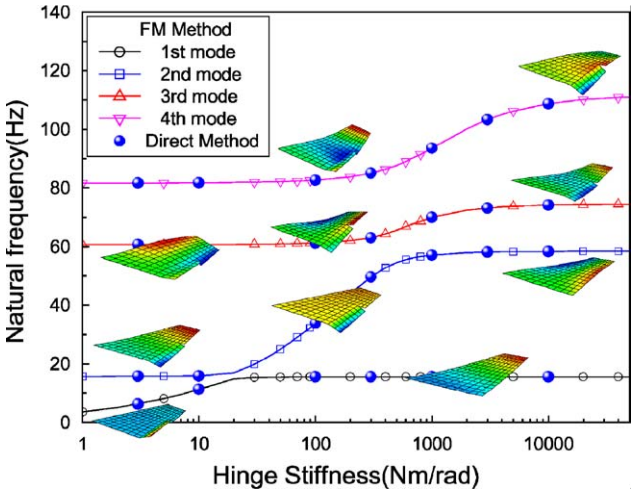

Fig. 4. Natural frequencies versus hinge stiffness.

Table 2
Comparison of flutter speeds and frequencies ($M = 0.7$, $K_\theta = 1000\,\mathrm{N\,m/rad}$)

	Flutter speed (m/s)	Flutter frequency (Hz)
NASTRAN	201.1	80.6
V-g(Direct)	196.9	79.7
V-g(FM)	197.1	79.6
Root-locus(FM)	196.9	79.6
Time(FM)	197.0	79.7

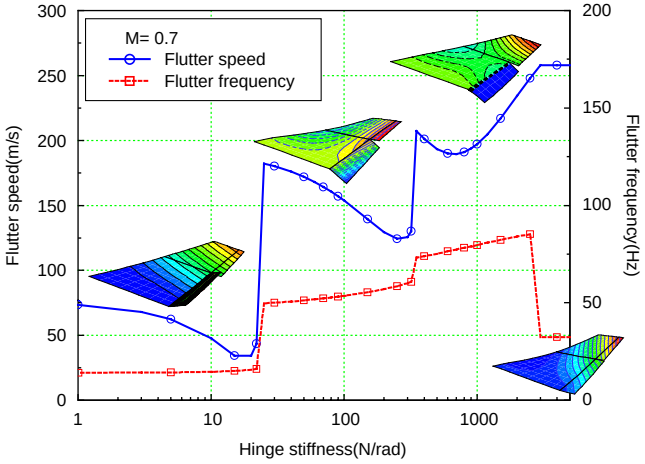

Fig. 5. Flutter speed and frequency for various hinge stiffness.

flutter results for $K_\theta = 1000\,\mathrm{N\,m/rad}$ are in good agreement with those of Reference (MacNeal-Schwendler Corp, 1981). Fig. 5 shows the flutter speeds and frequencies for various hinge stiffness values. This figure provides us the important information of both linear and nonlinear aeroelastic characteristics. As shown in Fig. 5, the aeroelastic characteristics of an aircraft wing with a control surface significantly vary and jumps in the flutter speed and frequency are observed. These jumps are due to the change in the flutter mode. The hinge stiffness values at which these jumps

occur are almost the same as those for the mode shape changes in Fig. 4. And also, there is not a flutter solution in the airspeed region from 75 to 125 m/s and from 175 to 185 m/s.

The flutter characteristics in Fig. 5 can be subdivided into four regions. The first is the bending–flapping mode coalescent flutter and the second is the hump mode flutter of the third mode (torsion–flapping mode). The third is the third-fourth mode (first torsion–second bending mode) coalescent flutter and the last is the first-second mode (first bending–first torsion) coalescent flutter. Fig. 3 shows that the hinge stiffness decreases due to the existence of structural nonlinearities such as free-play and bilinearity. Therefore, we can predict that the nonlinear flutter boundary is lower than that of the linear case. For more than approximately 3000 N m/rad, the flutter characteristics are similar to that of a clean wing. The hinge stiffness used in the following nonlinear aeroelastic analysis is 3000 N m/rad and free-play angle is 0.125°.

3.3. Aeroelastic analysis (free-play case, $a = 0.0$)

Fig. 6 shows the LCO amplitudes of an aircraft wing with free-play nonlinearity observed in the nonlinear aeroelastic analysis. Fig. 7 shows the parameter map of the aircraft wing with free-play nonlinearity. The parameter map shows the aeroelastic responses for various air speeds and initial conditions. The first mode of the numerical model is a rigid body mode of a flap. Thus, to change the initial condition, the displacement of the first mode is excited in the present study. The type of LCO is dependent on the energy level of the system. Changing the initial condition changes the energy level of the system. Three types of stable LCO and unstable LCO are observed for air speeds below the linear flutter boundary. Stable LCOs can be subdivided into LCO 1, LCO 2, and LCO 3 dependent on the LCO mode shape. The LCO flutter modes of LCO 1, LCO 2, and LCO 3 are the bending–flapping mode, the torsion–flapping mode (hump mode), and the first torsion–second bending mode, respectively.

LCO 3, with a large LCO amplitude, can be predicted in the frequency-domain analysis whereas LCO 1 and LCO 2 cannot be observed. At low air speeds, it is observed that LCO 1 is independent of the initial condition and the amplitudes are nearly constant. For air speeds between approximately 125 and 200 m/s, different types of LCO are observed in the same air speed dependent on an initial condition. For air speeds between approximately 175 and 200 m/s, periodic motions can be observed. Periodic motion is defined as the oscillation including several harmonics. For air speeds between approximately 200 and 250 m/s, LCO 3 and unstable LCO can be observed. The types of aeroelastic responses can be dependent on the initial condition. Unstable LCO can cause the instability of the aeroelastic system whereas stable LCO does not. The aeroelastic responses in Fig. 6 do not become unstable due to the initial condition because the amplitude of stable LCO is larger than that of unstable LCO.

Figs. 8–13 show the time history and phase plot for the wing tip and flap. Figs. 8 and 9 show that two different types of LCO occur when the air speed is 160 m/s. One is LCO 1 with low frequency (20.0 Hz) and the other is LCO 2 with high frequency (60.9 Hz). Due to the difference of the flutter mode, the tip amplitude of LCO 1 is larger than that of LCO 2 whereas the flap amplitudes of LCO 1 and LCO 2 are almost the same. These LCO types are dependent on an initial flap amplitude. Figs. 10 and 11 show two different types of aeroelastic responses dependent on the initial amplitude when the air speed is 180 m/s. In this air speed, two types of LCOs are observed. When the initial flap angle ratio (θ_0/δ) is 1.5, periodic motion with several frequencies including 9, 20, and 60 Hz is observed. When the initial flap

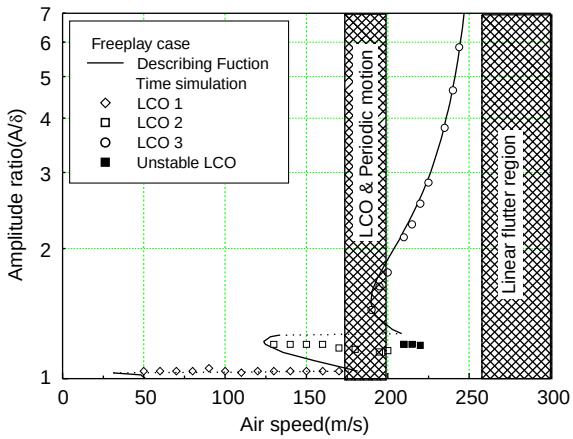

Fig. 6. LCO amplitudes of aircraft wing with free-play nonlinearity.

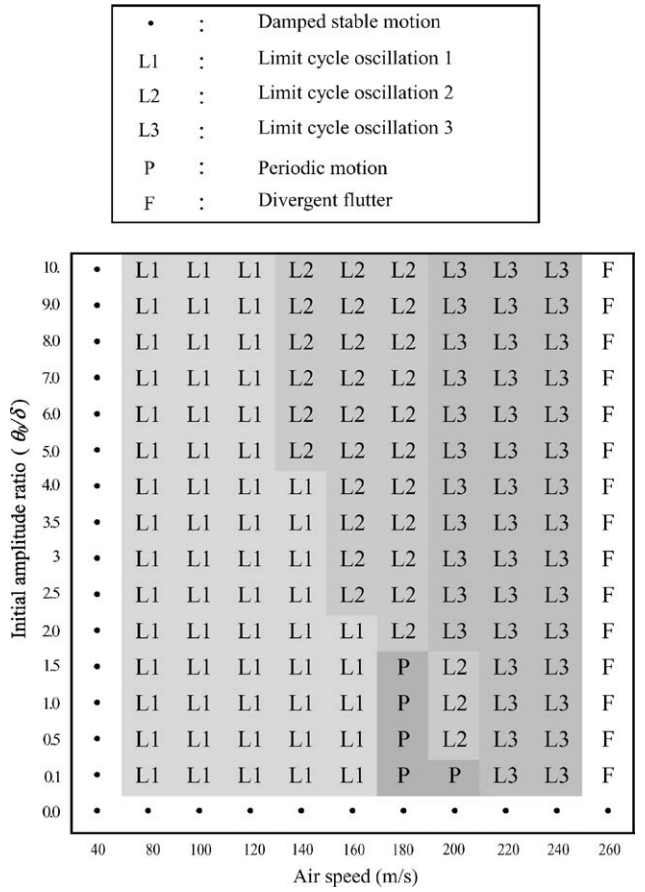

Fig. 7. Parameter map of aircraft wing with free-play nonlinearity.

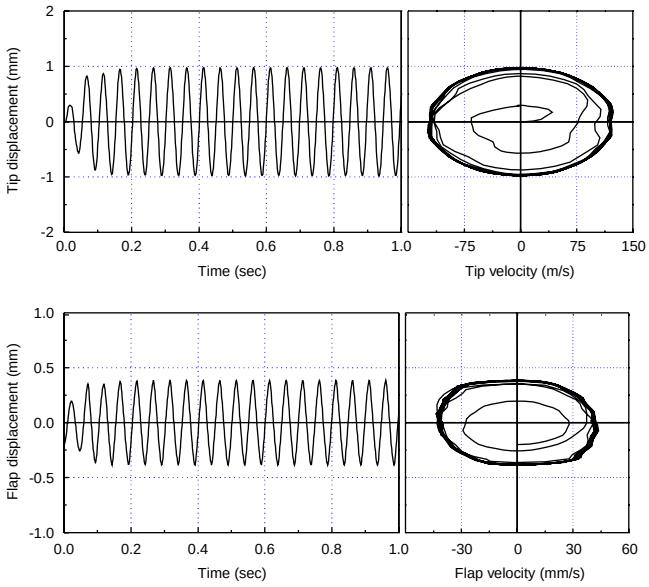

Fig. 8. Aeroelastic responses of LCO 1 ($U = 160\,\mathrm{m/s}$, $\theta_0/\delta = 1.0$).

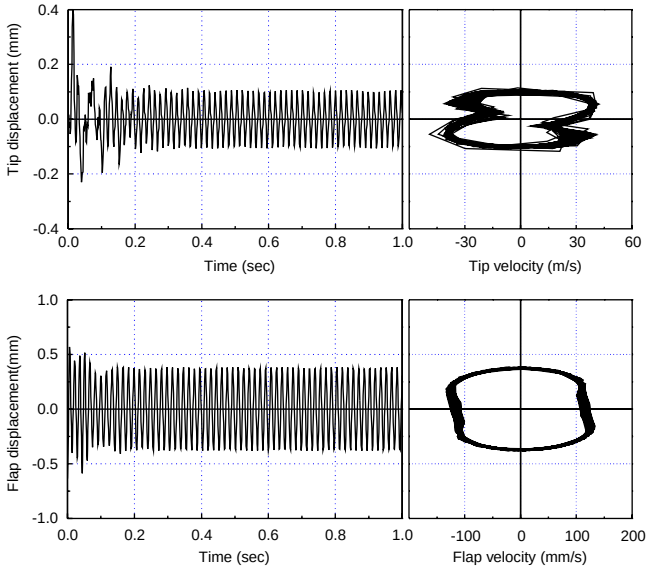

Fig. 9. Aeroelastic responses of LCO 2 ($U = 160\,\mathrm{m/s}$, $\theta_0/\delta = 3.2$).

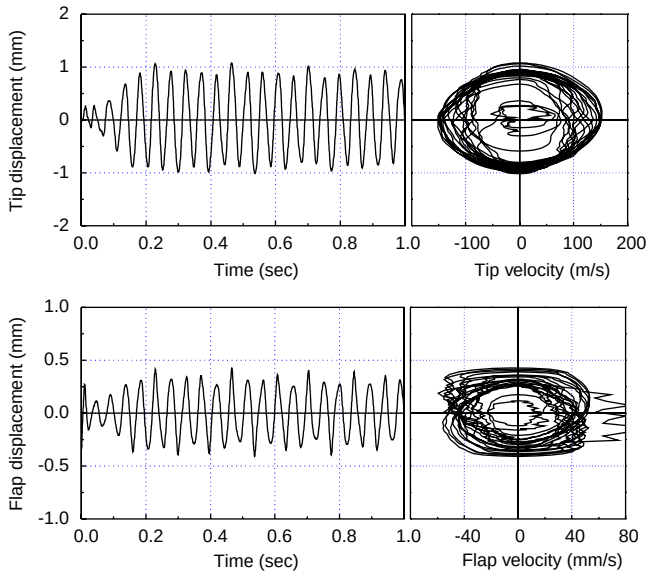

Fig. 10. Aeroelastic responses of periodic motion ($U = 180\,\mathrm{m/s}, \theta_0/\delta = 1.5$).

angle ratio is more than 2.0, LCO 2 is observed and is similar to that in Fig. 9. Figs. 12 and 13 show the aeroelastic responses when the air speed is 210 m/s. Fig. 12 shows that an unstable LCO with several frequencies disappears and then LCO 3 with large amplitude remains when the initial amplitude ratio is 1.6. Due to the existence of LCO 3, the aeroelastic system remains stable independent of the initial condition. Fig. 13 shows that LCO 3 is observed when the initial amplitude ratio is 2.4. The flutter frequency of LCO 3 is 80.9 Hz and the flutter mode is the first torsion–second bending mode. The amplitude of LCO 3 increases as the air speed increases. Aeroelastic responses over the linear flutter boundary are unstable independent of the initial condition.

3.4. Aeroelastic analysis (bilinear case, a = 0.1)

In the previous section, various kinds of LCOs due to free-play were observed in a wide range of air speeds. In this section, the effects of the stiffness aK_θ on the free-play LCO characteristics will be investigated. Fig. 14 shows the LCO

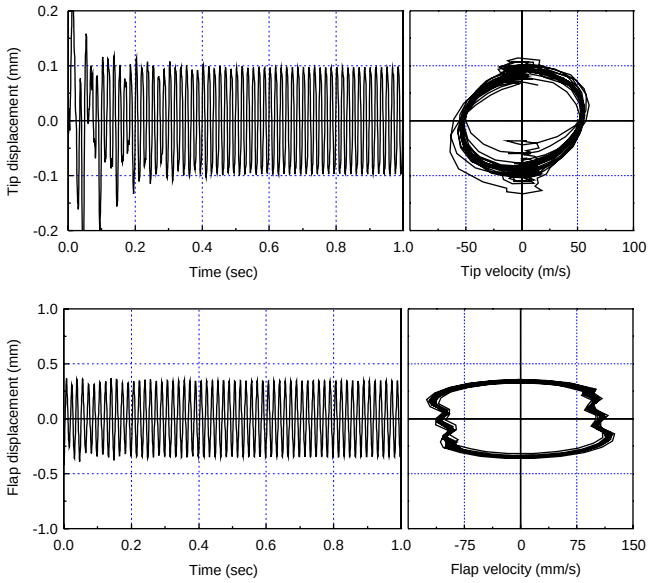

Fig. 11. Aeroelastic responses of LCO 2 ($U = 180$ m/s, $\theta_0/\delta = 2.0$).

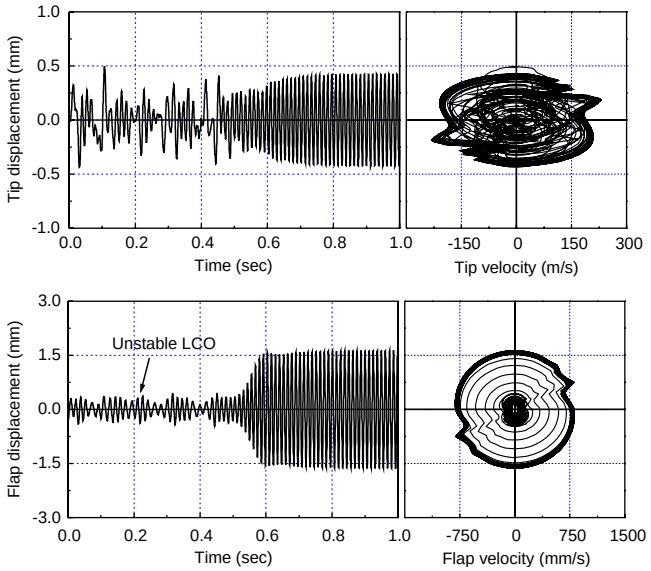

Fig. 12. Aeroelastic responses of unstable LCO and LCO 3 ($U = 210$ m/s, $\theta_0/\delta = 1.6$).

amplitudes of an aircraft wing with bilinear nonlinearity. As shown in Fig. 3, the equivalent stiffness of a bilinear spring is larger than that of free-play nonlinearity because the stiffness ratio a is not zero. The hinge stiffness in free-play is 300 N m/rad. Fig. 15 shows the parameter map of an aircraft wing with bilinear nonlinearity. Two types of LCO and unstable LCO are observed for air speeds below the linear flutter boundary. LCO 1 is not observed because the equivalent stiffness of a bilinear spring is larger than 300 N m/rad. As shown in Fig. 5, the bending–flapping mode flutter similar to LCO 1 occurs when the equivalent stiffness is less than 30 N m/rad. For free-play nonlinearity, LCO 1 can be observed when the equivalent stiffness is very small. For air speeds between approximately 125 and 175 m/s, LCO 2 (about 60 Hz) with a small amplitude is observed independent of the initial amplitude. This LCO is the same as the LCO 2 of the free-play case.

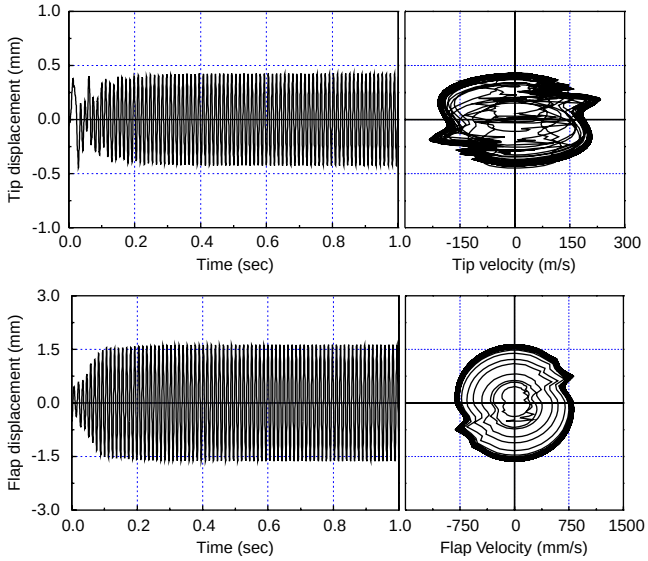

Fig. 13. Aeroelastic responses of LCO 3 ($U = 210$ m/s, $\theta_0/\delta = 2.4$).

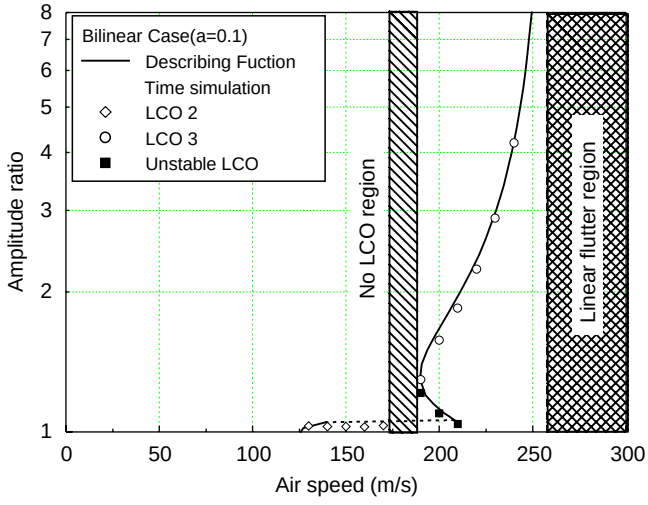

Fig. 14. LCO amplitudes of aircraft wing with bilinear nonlinearity ($a = 0.1$).

Figs. 16–19 show the time history and phase plot. Fig. 16 shows the aeroelastic response when the air speed is 160 m/s. For air speeds between approximately 175 and 185 m/s, no type of LCO is observed. Fig. 17 shows the aeroelastic responses when the air speed is 180 m/s. Although the damping is small, the oscillation damps out. When the air speed is larger than about 185 m/s, LCO 3 and unstable LCO are observed dependent on the initial amplitude. Fig. 18 shows that unstable LCO with small amplitude disappears while the LCO 3 remains when the air speed is 200 m/s and the initial amplitude ratio is 1.21. When the initial amplitude ratio is less than this value, unstable LCO disappears and LCO 3 does not occur. Fig. 19 shows the aeroelastic response when the air speed is 230 m/s. LCO 3 with large amplitude is observed independent of the initial amplitude. Periodic motion shown in Fig. 10 is not observed for the bilinear case.

In Figs. 6 and 20, there are two interesting regions. One is the region of "LCO and periodic motion (Region 1)" in Fig. 6 and the other is the region of "No LCO region (Region 2)" in Fig. 14. It appears that these two regions are related to the change in the LCO flutter mode type. In Fig. 5, there are two minimum flutter speed points in $K_\theta = 20$ N m/rad and $K_\theta = 300$ N m/rad. The flutter speed and frequency of $K_\theta = 20$ N m/rad are approximately 30 m/s and 20 Hz, respectively. Those of $K_\theta = 300$ N m/rad are approximately 125 m/s and 60 Hz. These frequencies are similar to

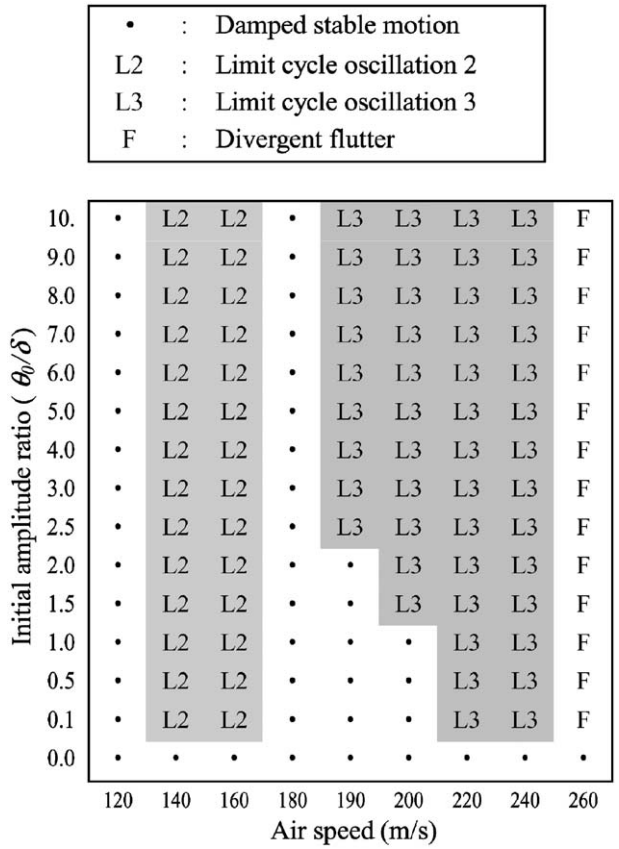

Fig. 15. Parameter map of aircraft wing with bilinear nonlinearity ($a = 0.1$).

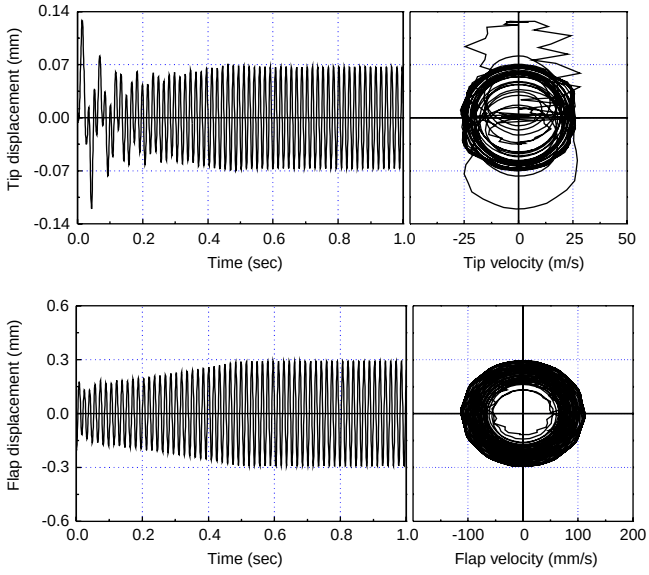

Fig. 16. Aeroelastic responses of LCO 2 ($U = 160\,\mathrm{m/s}$, $\theta_0/\delta = 1.0$).

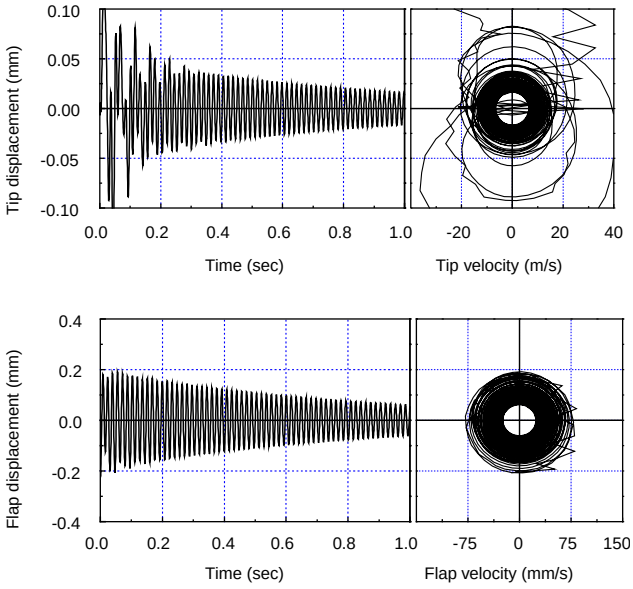

Fig. 17. Aeroelastic responses of LCO 2 ($U = 180$ m/s, $\theta_0/\delta = 1.0$).

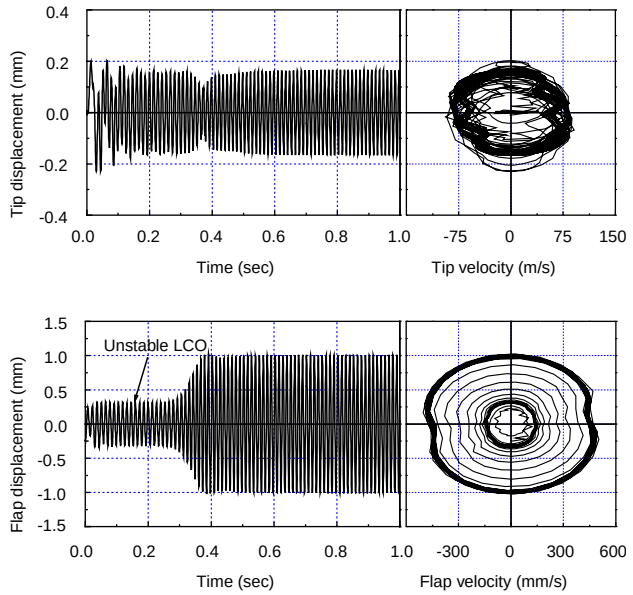

Fig. 18. Aeroelastic responses of unstable LCO and LCO 3 ($U = 200$ m/s, $\theta_0/\delta = 1.21$).

those of stable LCO 1 and LCO 2. The lowest three frequencies of Fig. 10 are approximately 9, 21, and 52 Hz, respectively. Hence, there are three types of stable LCOs in Region 1 whereas unstable LCOs disappear. The characteristics of the Region 2 are similar to those of Region 1 but the LCO and periodic motion are not observed.

Fig. 20 shows the LCO amplitudes of an aircraft wing with free-play and bilinear nonlinearities. The LCO boundary of free-play nonlinearity is lower than that of bilinear nonlinearity. When the stiffness ratio a is 0.1, LCO 1 and periodic motion are not observed. When the stiffness ratio a is 0.2, LCO 1, LCO 2, and an unstable LCO are not observed. Thus, periodic motions in the present study are mainly caused by free-play. Also, the LCO amplitude of the bilinear case is smaller than that of the free-play case. Therefore, the aeroelastic characteristics of an aircraft wing with a control surface become better as the stiffness within free-play increases.

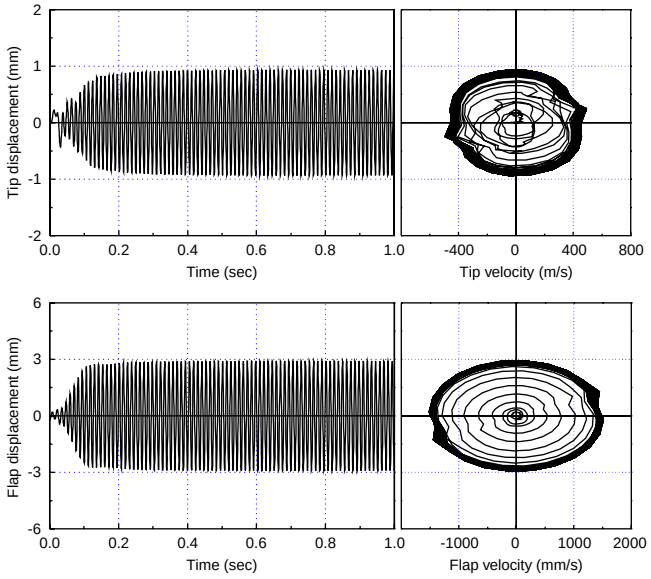

Fig. 19. Aeroelastic responses of LCO 3 ($U = 230\,\mathrm{m/s}$, $\theta_0/\delta = 1.0$).

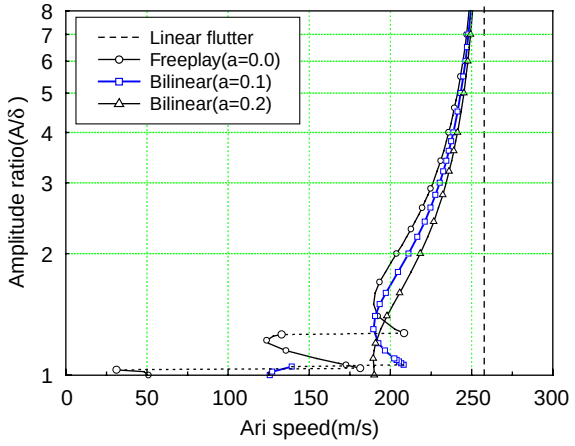

Fig. 20. Comparison of nonlinear aeroelastic characteristics for different nonlinearities.

4. Conclusions

In the present study, the nonlinear aeroelastic analysis of an aircraft wing with a control surface is performed. The finite element method is used for the free vibration analysis of an aircraft wing. A modal approach using the fictitious mass method is used to save computation time and memory. The doublet-hybrid method is used for the calculation of subsonic unsteady aerodynamic forces and the minimum-state approximation is used for the approximation of unsteady aerodynamic forces. The structural nonlinearity in the control surface hinge is assumed by free-play and bilinear nonlinearities and is linearized using the describing function. The nonlinear aeroelastic analysis is conducted in the frequency- and time-domain.

From free vibration analysis the vibration characteristics of an aircraft wing with a control surface vary considerably with hinge stiffness. For the free-play case, three types of LCO, unstable LCO, and periodic motion are observed dependent on the initial conditions for air speeds below the linear flutter boundary. These various aeroelastic responses are due to the change of flutter mode. Although the flap hinge stiffness is so large, the nonlinear aeroelastic responses like LCO are observed due to free-play. For the bilinear case, two different types of LCO and unstable LCO are observed for air speeds below the linear flutter boundary. Periodic motion is not observed and there exists an air speed

region where LCO is not observed. The nonlinear aeroelastic characteristics of an aircraft wing with a control surface become better as the stiffness within free-play increases.

Acknowledgements

This research was supported by Agency for Defense Development (ADD) and the Ministry of Science and Technology (National Research Laboratory Program) in the Republic of Korea. This support is gratefully acknowledged. And also, the authors appreciate the review and comments of Mr Christopher O. Johnston of Virginia Tech about this paper and express special thanks to the associate Editor Dr Earl H. Dowell and reviewers for many valuable comments and suggestions.

References

Bae, J.S., 2002. Aeroelastic characteristics and flutter suppression considering structural nonlinearity. Ph.D Dissertation, Department of Aerospace Engineering. Korea Advanced Institute of Science Technology.

Bae, J.S., Lee, I., 2004. Limit cycle oscillation of missile control fin with structural nonlinearity. Journal of Sound and Vibration 269 (3–5), 669–687.

Bae, J.S., Yang, S.M., Lee, I., 2002. Linear and nonlinear aeroelastic analysis of fighter-type wing with control surface. Journal of Aircraft 39, 697–708.

Bae, J.S., Kim, D.K., Shin, W.H., Lee, I., Kim, S.H., 2004. Nonlinear aeroelastic analysis of deployable missile control fin. Journal of Spacecraft and Rockets 41 (2), 264–271.

Conner, M.D., Tang, D.M., Dowell, E.H., Virgin, L.N., 1997. Nonlinear behavior of a typical airfoil section with control surface free-play: a numerical and experimental study. Journal of Fluids and Structures 11, 89–109.

Evesman, W., Pitt, D.M., 1991. Lattice/doublet point method for lifting surfaces in subsonic flow. AIAA Journal 28, 572–578.

Hauenstein, A.J., Laurenson, R.M., Eversman, W., Galecki, G., Qumei, I., 1990. Chaotic response of aerosurfaces with structural nonlinearities. AIAA Paper 90-1034-CP, AIAA/ASME/ASCE/AHS/ASC 31st Structures, Structural Dynamics and Materials Conference, Long Beach, CA, USA.

Karpel, M., 1982. Design for active flutter suppression and gust alleviation using state-space aeroelastic modeling. Journal of Aircraft 19, 221–227.

Karpel, M., Newman, M., 1988. Efficient vibration mode analysis of aircraft with multiple external store configurations. Journal of Aircraft 25, 747–751.

Laurenson, R.M., Trn, R.M., 1980. Flutter analysis of missile control surface containing structural nonlinearities. AIAA Journal 18, 1245–1251.

Lee, C.L., 1986. An iterative procedure for nonlinear flutter analysis. AIAA Journal 18, 1245–1251.

Lee, B.H.K., Tron, A., 1989. Effects of structural nonlinearities on flutter characteristics of the CF-18 aircraft. Journal of Aircraft 26, 781–786.

Lee, I., Kim, S.H., 1995. Aeroelastic analysis of a flexile control surface with structural nonlinearity. Journal of Aircraft 32, 868–874.

MacNeal-Schwendler Corp. (MSC), Los Angeles, CA, 1981. MSC/NASTRAN User's Manual.

Sheta, E.F., Harrand, V.J., Thomson, D.E., Strganac, T.W., 2002. Computational and experimental investigation of limit cycle oscillations of nonlinear aeroelastic systems. Journal of Aircraft 39, 133–141.

Tang, D.M., Dowell, E.H., Virgin, L.N., 1999. Limit cycle behavior of an airfoil with a control surface. Journal of Fluids and Structures 12, 839–858.

Tang, D.M., Kholodar, D., Dowell, E.H., 2000. Nonlinear response of airfoil section with control surface free-play to gust loads. AIAA Journal 38, 1543–1557.

Ueda, T., Dowell, E.H., 1982. A new solution method for lifting surfaces in subsonic flow. AIAA Journal 20, 348–355.

Virgin, L.N., Conner, M.D., Dowell, E.H., 1999. In the evolution of deterministic non-periodic behavior an airfoil. International Journal of Nonlinear Mechanics 34, 499–514.

Woolston, D.S., Runyan, H.W., Andrews, R.E., 1957. An investigation of effects of certain type of structural nonlinearities on wing and control surface flutter. Journal of Aeronautical Sciences 24, 57–63.

Yang, Z.C., Zhao, L.C., 1988. Analysis of limit cycle flutter of an airfoil in incompressible flow. Journal of Sound and Vibration 123, 1–13.

Zara, J., Haenstein, A.J., Laurenson, R.M., Eversman, W., Qumei, I., 1992. Caotic and nonlinear response of aerosurfaces with structural nonlinearities. AIAA Paper 92-2547-CP, AIAA/ASME/ASCE/AIAS/ASC 33rd Structures, Structural Dynamics and Materials Conference.